Table of Contents

List of Tables

List of Figures

Chapter 4.   Solar Resource

4.1   The Sun

Aside from supporting virtually all life on Earth, the Sun is the energy source that drives the climate and weather on the entire planet. The heat and light that reaches Earth from the Sun account for over 99.9 percent of the available renewable energy used today, including solar-based resources such as: wind and wave power, hydroelectricity and biomass.

To better understand the solar resource as a means of harvesting it for energy production, several of the Sun's characteristics must be studied, such as: *geometry, the energy available (radiation), resource estimation and variability*. Acknowledging these characteristics provide a basis for understanding, using and predicting solar radiation data.

4.2   Solar Geometry

There are several geometrical relationships between the Sun and the plane where solar radiation is of interest. The most relevant are:

- **n**, day of the year.

- **Latitude (ϕ),** angular location north or south of the equator, being north positive.

- **Declination (δ),** angular position of the sun at solar noon with respect to the equator's plane, being north positive.

$$\delta = 23.45 \sin\left(\frac{360(284 + n)}{365}\right)$$

- **Hour angle (ω),** angular displacement of the Sun east or west of the local meridian at 15° per hour, being positive in the morning.

- **Zenith angle (θ_z),** angle between the vertical and the line to the Sun or angle of incidence of beam radiation on a horizontal surface.

$$\theta_z = \cos^{-1}\left[\cos\phi\cos\delta\cos\omega + \sin\phi\sin\delta\right]$$

- **Solar altitude angle (α_s),** angle between the horizontal and the line to the Sun.

$$\alpha_s = \sin^{-1}\left[\cos\phi\cos\delta\cos\omega + \sin\phi\sin\delta\right]$$

- **Solar azimuth angle (γ_s),** angular displacement form south of the projection of beam radiation on the horizontal plane, being west of south positive.

$$\gamma_s = sign(\omega)\left|\cos^{-1}\left[\frac{\cos\theta_z\sin\phi - \sin\delta}{\sin\theta_z\cos\phi}\right]\right|$$

Some of these are shown in Figure 4.1.
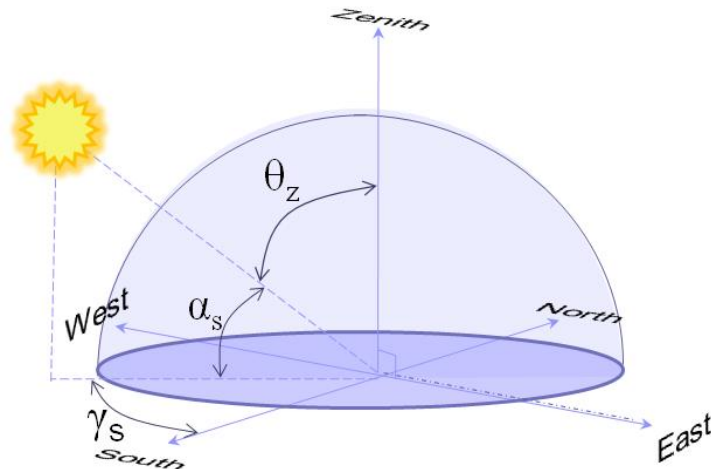
Figure 4.1 Solar geometry with respect to horizontal surface (Source: Adapted from [4])

4.3 Energy Available (Radiation)

The energy received from the Sun can be measured just outside the atmosphere or on a plane at Earth's surface. The solar constant is the amount of power that the Sun deposits per unit area exposed to sunlight and is equal to approximately 1,370 W/m^2 just outside Earth's atmosphere. Sunlight on Earth's surface is attenuated by the atmosphere to around 1,000 W/m^2 in clear sky conditions when the Sun is near the zenith. The extraterrestrial radiation however, is the one that would be received in the absence of Earth's atmosphere.

On Earth's surface, radiation can be categorized as being beam, diffuse or global. Beam or direct radiation refers to the radiation received from the Sun without having been scattered by the atmosphere. Diffuse radiation is the one whose direction has been changed by scattering in the atmosphere due to clouds, water vapor, trees, etc. Global or total radiation is the sum of these two.

4.3.1 How radiation is measured

It's important to recognize that there are two common methods which characterize solar radiation: the solar radiance or radiation, and solar insolation. Solar radiation is an

instantaneous power density in units of kW/m^2. The solar radiance varies throughout the day from 0 kW/m^2 at night to a maximum of about 1 kW/m^2. The solar radiance is strongly dependant on location and local weather. Solar radiance measurements consist of global radiation measurements taken periodically throughout the day. The measurements are taken using either a pyranometer, which is an instrument capable of measuring global radiation, or a pyrheliometer which measures beam radiation.

Solar insolation however, is the most commonly measured solar data. The solar insolation is the total amount of solar energy received at a particular location during a specified time period, for example kWh/m^2 day. While the units of solar insolation and solar irradiance are both a power density, solar insolation is different than the solar irradiance as the solar insolation is the instantaneous solar irradiance averaged over a given time period. Solar insolation data is commonly used for simple system design while solar radiance is used in more complicated systems to calculate its performance at each point in the day. Solar insolation can also be expressed in units of MJ/m^2 per year. The most common conversion units found in literature are shown in Table 4.1.

Table 4.1 Solar Data Conversion Table

Solar Radiation Conversions	
1 kWh/m^2	1 Peak Sun Hour
1 kWh/m^2	3.6 MJ/m^2
1 kWh/m^2	0.0116 Langley
1 kWh/m^2	860 cal/m^2
1 $MJ/m^2/day$	0.01157 kW/m^2
1 kW/m^2	100 mW/cm^2

4.3.2 Calculating beam and diffuse radiation from measured global data

As was stated before, radiation data is usually measured with pyranometers capturing the global insolation. Several models have been developed to separate the beam and

diffuse components from the global insolation. The one adopted for the purpose of this investigation is the one presented in Solar Engineering of Thermal Processes by Duffie. These calculations are often done using the ratio of monthly (measured) available radiation $\overline{H}$ to the theoretically possible (monthly extraterrestrial radiation) $\overline{H}_0$. This ratio is known as $\overline{K}_T$, or the average clearness index. The following expression are all from Duffie.

$$\overline{K}_T = \frac{\overline{H}}{\overline{H}_0}$$

The monthly extraterrestrial radiation is calculated as follows:

$$\overline{H}_0 = \frac{24(3600)G_{SC}}{\pi} \times \left(1 + 0.033\cos\frac{360n}{365}\right) \times \left(\cos\phi\cos\delta\sin\omega_s + \frac{\pi\omega_s}{180}\sin\phi\sin\delta\right)$$

where G_{sc} is the solar constant, n is the average day of the month, ϕ is the latitude, δ is the declination angle and ω_s is the sunset hour angle.

After calculating $\overline{K}_T$, the diffuse and beam components can be calculated according to the average diffuse fraction given by:

$$\frac{\overline{H}_d}{\overline{H}} = 1.311 - 3.022\overline{K}_T + 3.42\overline{K}_T^2 - 1.821\overline{K}_T^3 \quad for \ \omega_s > 81.4°$$

where $\overline{H}_d$ is the monthly average daily diffuse radiation calculated by:

$$\overline{H}_d = \overline{H}(1.311 - 3.022\overline{K}_T + 3.42\overline{K}_T^2 - 1.821\overline{K}_T^3)$$

thus, the monthly average daily beam radiation is:

$$\overline{H}_b = \overline{H} - \overline{H}_d$$

4.4 Resource estimation

There have been several proposed methodologies for estimating solar radiation in the past. These take into account factors such as: hours of bright sunshine, hours of cloudiness, atmospheric attenuation of solar radiation by scattering or absorption, average clear-sky daily radiation and empirical constants dependent on location to name a few.

Under partly cloudy skies, due to the random and unknown location of the clouds, no model can accurately estimate the solar radiation incident on the earth's surface at any given time and location. These models, far from being useful, provide means for ambiguity according to some experts due to the fact that sunshine or cloudiness data are usually based on visual observations and there is uncertainty as to what constitutes a clear or partly cloudy day.

One of the most used methods for estimating solar radiation is the meteorological-statistical (METSTAT) solar radiation model developed by the National Solar Radiation Database (NSRDB). It is used to estimate solar radiation when measured data were not available reproducing the statistical and stochastic characteristics of multiyear solar radiation data sets. This sacrifices accuracy for specific hours so; modeled values for individual hours may differ greatly from measured values if they had been made.

According to NSRDB, it is important that simulated data sets accurately represent the following statistical and stochastic characteristics of measured data: monthly moments (such as: mean, variance, skewness, kurtosis), monthly cumulative frequency distributions (cfds), diurnal and seasonal patterns, hourly and daily autocorrelations, cross-correlations between elements (global horizontal, diffuse horizontal, direct normal) and persistence.

Several features incorporated in the model were: hourly calculations using hourly total and opaque cloud cover, hourly precipitable water vapor, daily aerosol optical depth, and daily albedo input data. Figure 4.2 is a representation of the NSRDB algorithms.

These produce representative diurnal and seasonal patterns, daily autocorrelations, and persistence. Placing the statistical algorithms between the input data and the deterministic algorithms leads to proper cross-correlations between the direct normal, diffuse horizontal and global horizontal components.

Even though these methods are available for resource estimation, the best estimation that can be done is using available measured data from a location near the point of interest.
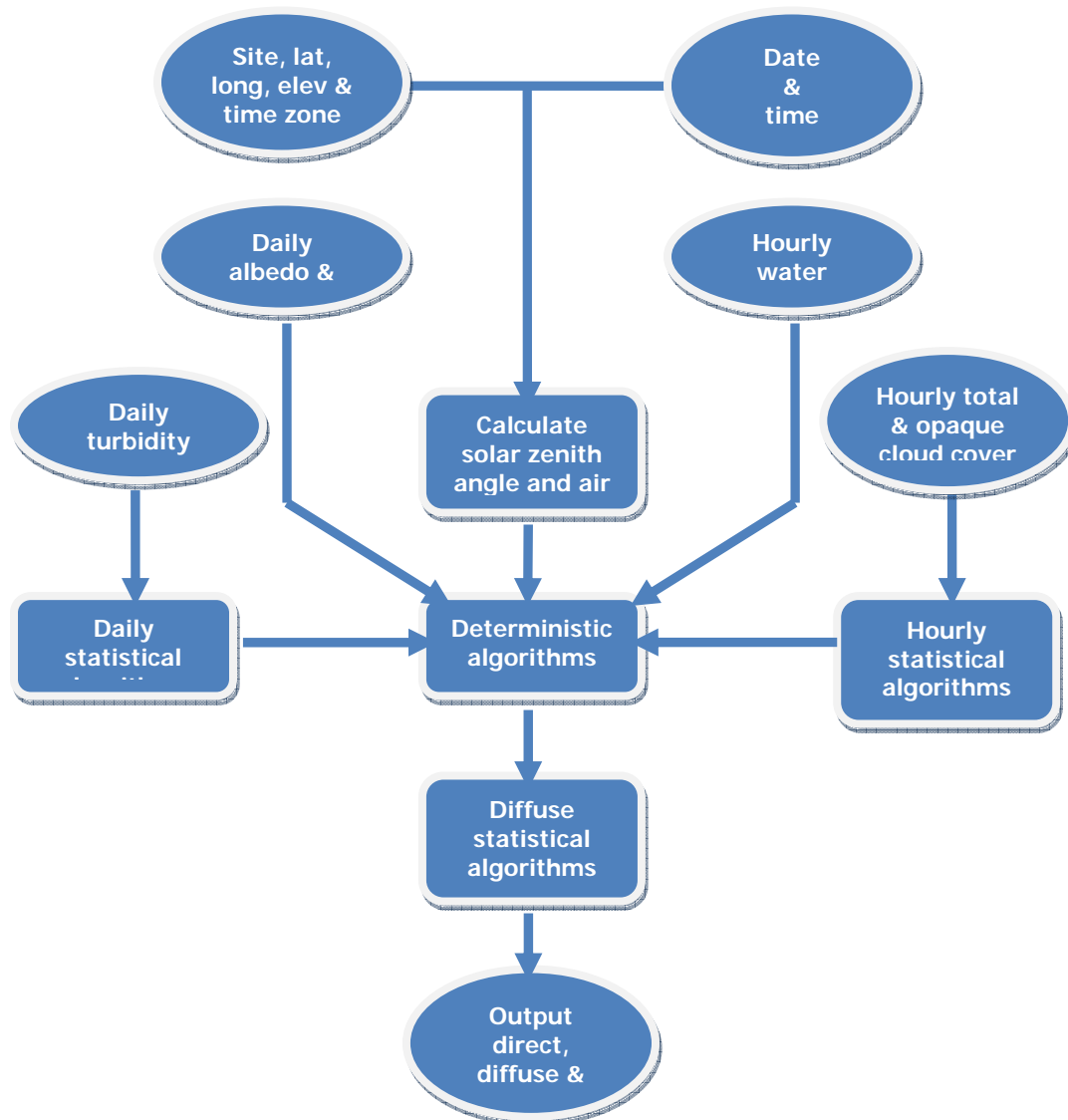
Figure 4.2: NSRDB algorithms for resource estimation (Source: Adapted from [7])

4.5   Variability of solar data

Solar variations are changes in the amount of radiant energy emitted by the Sun. It has been typically attributed to two main factors: the solar cycle and Earth's atmosphere.

The total solar irradiance (TSI) is the amount of solar radiative energy impinging on the Earth's upper atmosphere. It is observed to vary in phase with the solar cycle, with

yearly averages going from 1365.5 Watt per square meter at solar minimum, up to of 1366.6 at solar maximum, with fluctuations about the means of about +/- 1 Watt per square meter on timescales of a few days as shown in Figure 4.3. Variation at the 0.1% level is far too small to affect Earth's climate, but it is worth keeping in mind that continuous reliable measurements of the TSI are only available since 1978; the minimum and maximum levels of solar activity have remained roughly the same from then to now.
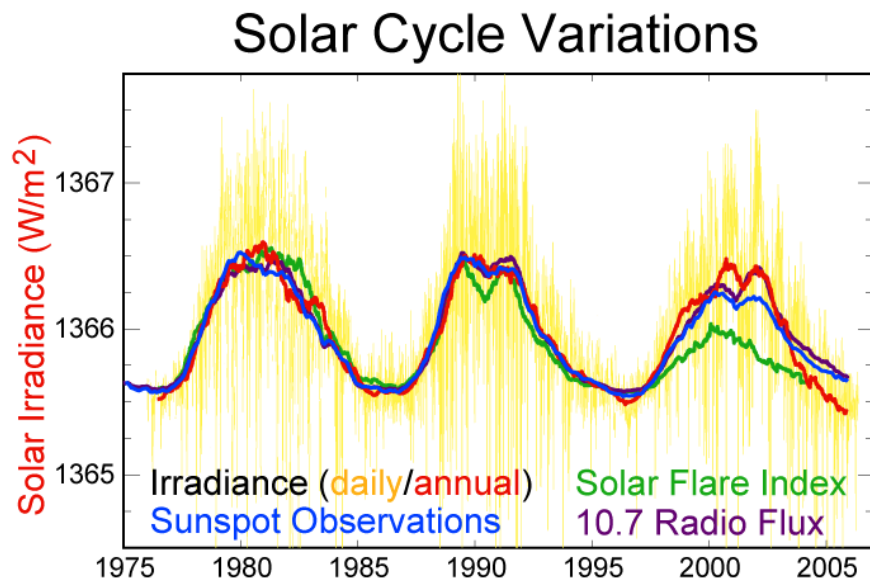
Figure 4.3: Solar cycle variations 1975-2005 (Author: Robert A. Rohde [24])

Figure 4.3 contains the last three solar cycles as measured in solar irradiance and sunspot numbers. Solar irradiance at the top of the Earth's atmosphere is presented as daily and annual averages. The 11 year solar cycle is a fundamental aspect of the sun's behavior and is associated with variations in total output and activity. Irradiance measurements have only been available during the last three cycles and are based on a composite of many different observing satellites and instruments.

Solar variability also occurs due to: changes in extraterrestrial radiation, atmospheric scattering (by air, water and dust) or atmospheric absorption (by ozone, water and carbon dioxide). There is some evidence that sunshine at the Earth's surface has been decreasing in the last 50 years possibly caused by increased atmospheric pollution.

4.6   Uncertainty of solar data

As with the use of any measuring device, there is always a level of uncertainty as to whether the data being measured can be considered accurate. Myers, Emery, and Stoffel (1989) and Wells (1992) identified the major sources of error associated with pyranometers and pyrheliometers. The most significant measurement errors were associated with properties of these instruments, their calibration and their data acquisition systems.

Errors introduced by the instrument include: deviations from cosine law response to incident radiation, ambient temperature effects on response to radiation, nonlinear response to incident radiation, non-uniform response across the solar spectrum and errors associated with the use of shadow bands for measuring diffuse radiation.

Errors introduced by calibration include: uncertainty in the definition of the international scale of solar radiation, errors in the transfer of the World Radiometric Reference to the secondary reference instruments and errors in the calibration of individual instruments.

The results of the work of Myers, Emery, and Stoffel (1989) and Wells (1992) yielded the following levels of uncertainty: global horizontal ± 5%, direct normal ± 3% and diffuse horizontal ± 7%.

4.7   Solar Resource and Data Availability in Puerto Rico

In this work solar data was gathered from five sources which account for eighteen different sites in Puerto Rico. The main data source is the previously published work of A.M. López and K.G. Soderstrom. This data collection project was conducted by the Center for Energy and Environment Research (CEER) in the University of Puerto Rico at Mayagüez and supported in part by the U.S. Department of Energy (DOE). The data

was measured with a PSP pyranometer on a horizontal plane between 1976 and 1981 for the municipalities of: Mayagüez, San Juan, Ponce, Cabo Rojo, Cataño and Manatí. A summary of the average daily global insolation is presented in Table 4.2.

Radiation data was also obtained through the U.S. Department of Agriculture Forest Service, Institute of Tropical Forestry in San Juan, P.R. The study, conducted by C.B. Briscoe, aimed at studying weather patterns in and near the Luquillo Mountains of Puerto Rico, better known as El Yunque Rainforest. Thirteen sites were selected to be studied and data was collected regarding temperature, humidity, wind and precipitation (rain). Solar radiation data was measured in only three of these sites: Fajardo, Río Grande and Gurabo. The average daily global insolation on a horizontal plane is shown in Table 4.3. Mean hourly insolation measurements were made between 1966 and 1967 in Langleys. We computed the averages per month and converted the data to MJ/m^2 (1 Langley = 0.041868 MJ/m^2) for ease of comparison.

Table 4.2 Average daily global insolation on a horizontal plane (MJ/m2) for Mayagüez, San Juan, Ponce, Cabo Rojo, Cataño and Manatí (Soderstrom)

Month	Mayagüez	San Juan	Ponce	Cabo Rojo	Cataño	Manatí
January	14.2	14.8	16.5	16.5	16	15.2
February	15.5	16.2	18.9	19.1	22.2	16.5
March	17.1	18	21.5	22.2	19	21.7
April	18	17.5	21.7	19.4	20.3	22
May	17.1	15.3	19.2	23.1	16.6	19.1
June	17.6	18.4	20	23.6	16.8	23.5
July	16.5	20.3	22.4	22.3	24.6	20.8
August	17.2	18.9	22	20.5	21	19
September	16.3	16.4	20.4	21.7	17.9	17.7
October	15.2	16	18.3	18.9	17	17.4
November	14.7	14.6	16.4	17.7	16.1	16.3
December	13.1	13	14.8	14.2	14.8	13.6

Table 4.3: Average daily global insolation on a horizontal plane (MJ/m^2)

for Fajardo, Rio Grande and Gurabo (USDA – Briscoe)

Month	Fajardo	Río Grande	Gurabo
January	15.9	10.0	17.0
February	20.0	12.1	19.5
March	20.6	13.7	13.4
April	19.8	9.1	21.4
May	25.1	12.1	22.3
June	12.6	12.1	21.2
July	24.3	12.5	19.6
August	11.4	13.8	18.5
September	21.1	13.2	13.5
October	8.8	10.3	11.8
November	17.1	6.2	23.9
December	12.7	6.4	12.6

Another source of data from Juana Diaz, Isabela and Lajas was supplied by Dr. Raúl Zapata from the Civil Engineering Department at the University of Puerto Rico. This was raw data in ASCII format collected every five minutes from 2000 to 2002. We processed the data to produce hourly average insolation tables. This data was then averaged to obtain monthly and yearly insolation and is presented in Table 4.4.

Table 4.4: Average daily global insolation on a horizontal plane (MJ/m^2) for

Juana Diaz, Isabela and Lajas (Zapata)

Month	Juana Diaz	Isabela	Lajas
January	17.9	16.5	13.6
February	20.5	19.3	17.1
March	23.4	21.1	21.2
April	21.0	15.6	20.2
May	22.6	23.2	19.9
June	20.9	21.0	19.2
July	21.1	21.7	19.3
August	18.4	20.3	20.4
September	20.9	18.3	18.7
October	19.5	18.5	18.5
November	18.0	17.8	17.0
December	15.2	15.8	15.6

We obtained publicly available data for Aguadilla, Ceiba and Carolina from NREL's (National Renewable Energy Laboratory) National Solar Radiation Database. This data was collected and averaged hourly from 2002-2003 and was processed to produce monthly and yearly averages. The processed data is shown in Table 4.5.

Table 4.5: Average daily global insolation on a horizontal plane (MJ/m^2)
for Aguadilla, Ceiba and Carolina

Month	Aguadilla	Ceiba	Carolina
January	14.8	13.2	14.6
February	17.2	15.3	16.9
March	19.2	18.2	20.3
April	18.4	16.1	20.6
May	20.6	18.4	21.7
June	19.8	17.1	21.3
July	20.9	18.3	20.9
August	19.5	17.5	20.7
September	19.1	16.8	19.6
October	17.0	15.4	17.4
November	14.5	12.9	13.8
December	13.5	12.3	12.6

Data for the last three sites: Guilarte, Bosque Seco and Maricao, is shown in Table 4.6. This data was also obtained from the NRCS website. Although processed, the data from Guilarte and Maricao forests was not taken into consideration in the construction of the radiation map since this forest data bias the map, bringing insolation levels down. Mayagüez, Cabo Rojo, Bosque Seco and Lajas provide a good estimate of insolation in the area.

Table 4.6: Average daily global insolation on a horizontal plane (MJ/m^2) for

Guilarte, Bosque Seco and Maricao

Month	Guilarte	Bosque Seco	Maricao
January	5.4	13.9	10.1
February	7.4	16.6	12.0
March	6.6	19.8	10.0
April	6.3	18.6	9.6
May	6.0	19.9	7.5
June	6.4	20.2	8.3
July	6.0	20.5	10.9
August	6.2	19.5	8.6
September	7.0	17.4	11.1
October	6.3	19.3	10.2
November	5.5	15.3	11.6
December	5.2	16.5	10.0

4.7.1 Calculation of beam and diffuse components of radiation in Puerto Rico

Using the model from Solar Engineering of Thermal Processes we calculated extraterrestrial radiation, K_T, beam and diffuse components of radiation. The results are shown in Table 4.7 thru Table 4.10, all radiation in MJ/m^2. Section 4.7.2 includes graphs that provide a visual summary of these results.

Table 4.7: Global Radiation Data, $\overline{H}$ (MJ/m^2)

Month	Ponce	Cabo Rojo	Mayaguez	Manati	Cataño	San Juan	Fajardo	Río Grande	Gurabo
January	16.5	16.5	14.2	15.2	16	14.8	15.9	10	17.0
February	18.9	19.1	15.5	16.5	22.2	16.2	20.0	12.1	19.5
March	21.5	22.2	17.1	21.7	19	18	20.6	13.7	13.4
April	21.7	19.4	18	22	20.3	17.5	19.8	9.1	21.4
May	19.2	23.1	17.1	19.1	16.6	15.3	25.1	12.1	22.3
June	20	23.6	17.6	23.5	16.8	18.4	12.6	12.1	21.2
July	22.4	22.3	16.5	20.8	24.6	20.3	24.3	12.5	19.6
August	22	20.5	17.2	19	21	18.9	11.4	13.8	18.5
September	20.4	21.7	16.3	17.7	17.9	16.4	21.1	13.2	13.5
October	18.3	18.9	15.2	17.4	17	16	8.8	10.3	11.8
November	16.4	17.7	14.7	16.3	16.1	14.6	17.1	6.2	10.1
December	14.8	14.2	13.1	13.6	14.8	13	12.7	6.4	12.6
Annual Average	19.3	19.9	16.0	18.6	18.5	16.6	17.5	11.0	16.7

Month	Juana Diaz	Isabela	Lajas	Aguadilla	Ceiba	Guilarte	Carolina	Guanica	Maricao
January	17.9	16.5	13.6	14.8	13.2	5.4	14.6	13.9	10.1
February	20.5	19.3	17.1	17.2	15.3	7.4	16.9	16.6	12.0
March	23.4	21.1	21.2	19.2	18.2	6.6	20.3	19.8	10.0
April	21	15.6	20.2	18.4	16.1	6.3	20.6	18.6	9.6
May	22.6	23.2	19.9	20.6	18.4	6.0	21.7	19.9	7.5
June	20.9	21	19.2	19.8	17.1	6.4	21.3	20.2	8.3
July	21.1	21.7	19.3	20.9	18.3	6.0	20.9	20.5	10.9
August	18.4	20.3	20.4	19.5	17.5	6.2	20.7	19.5	8.6
September	20.9	18.3	18.7	19.1	16.8	7.0	19.6	17.4	11.1
October	19.5	18.5	18.5	17.0	15.4	6.3	17.4	19.3	10.2
November	18	17.8	17	14.5	12.9	5.5	13.8	15.3	11.6
December	15.2	15.8	15.6	13.5	12.3	5.2	12.6	16.5	10.0
Annual Average	20.0	19.1	18.4	17.9	16.0	6.2	18.4	18.1	10.0

Table 4.8: Calculated Extraterrestrial Radiation, $\overline{H}_0$ (MJ/m^2)

Month	Ponce	Cabo Rojo	Mayaguez	Manati	Catano	San Juan	Fajardo	Río Grande	Gurabo
January	28.002	27.961	27.901	27.781	27.776	27.762	27.807	27.829	27.874
February	31.529	31.497	31.449	31.354	31.350	31.339	31.375	31.392	31.428
March	35.260	35.260	35.260	35.260	35.260	35.260	35.260	35.260	35.260
April	38.010	38.007	38.003	37.995	37.994	37.993	37.996	37.998	38.001
May	39.036	39.047	39.064	39.096	39.097	39.101	39.089	39.083	39.071
June	39.117	39.134	39.160	39.211	39.213	39.219	39.200	39.191	39.172
July	38.922	38.937	38.958	39.001	39.002	39.007	38.991	38.984	38.968
August	38.219	38.222	38.227	38.235	38.236	38.237	38.234	38.232	38.229
September	36.108	36.096	36.077	36.039	36.037	36.033	36.047	36.054	36.068
October	32.519	32.491	32.449	32.367	32.363	32.354	32.385	32.400	32.431
November	28.761	28.723	28.665	28.552	28.547	28.534	28.577	28.597	28.640
December	26.895	26.853	26.789	26.664	26.658	26.644	26.691	26.714	26.761
Annual Average	34.365	34.352	34.333	34.296	34.294	34.290	34.304	34.311	34.325

Month	Juana Diaz	Isabela	Lajas	Aguadilla	Ceiba	Guilarte	Carolina	Guanica	Maricao
January	27.980	27.743	27.980	27.744	27.882	27.929	27.788	28.024	27.929
February	31.512	31.324	31.512	31.325	31.435	31.471	31.360	31.546	31.471
March	35.260	35.260	35.260	35.260	35.260	35.260	35.260	35.260	35.260
April	38.008	37.992	38.008	37.992	38.002	38.005	37.995	38.011	38.005
May	39.042	39.105	39.042	39.105	39.069	39.056	39.094	39.030	39.056
June	39.126	39.227	39.126	39.227	39.168	39.148	39.208	39.108	39.148
July	38.930	39.014	38.930	39.013	38.965	38.948	38.998	38.914	38.948
August	38.220	38.238	38.220	38.238	38.228	38.224	38.235	38.217	38.224
September	36.102	36.027	36.101	36.027	36.071	36.086	36.041	36.115	36.086
October	32.504	32.341	32.504	32.342	32.437	32.469	32.372	32.534	32.469
November	28.740	28.517	28.740	28.517	28.648	28.692	28.559	28.781	28.692
December	26.872	26.625	26.872	26.625	26.770	26.819	26.671	26.918	26.819
Annual Average	34.358	34.284	34.358	34.285	34.328	34.342	34.298	34.372	34.342

Table 4.9: Average clearness index, K_T

Month	Ponce	Cabo Rojo	Mayaguez	Manati	Catano	San Juan	Fajardo	Río Grande	Gurabo
January	0.589	0.590	0.509	0.547	0.576	0.533	0.572	0.359	0.610
February	0.599	0.606	0.493	0.526	0.708	0.517	0.637	0.385	0.621
March	0.610	0.630	0.485	0.615	0.539	0.510	0.584	0.389	0.381
April	0.571	0.510	0.474	0.579	0.534	0.461	0.521	0.239	0.563
May	0.492	0.592	0.438	0.489	0.425	0.391	0.642	0.310	0.571
June	0.511	0.603	0.449	0.599	0.428	0.469	0.321	0.309	0.541
July	0.576	0.573	0.424	0.533	0.631	0.520	0.623	0.321	0.502
August	0.576	0.536	0.450	0.497	0.549	0.494	0.298	0.361	0.485
September	0.565	0.601	0.452	0.491	0.497	0.455	0.585	0.366	0.375
October	0.563	0.582	0.468	0.538	0.525	0.495	0.272	0.318	0.363
November	0.570	0.616	0.513	0.571	0.564	0.512	0.598	0.217	0.352
December	0.550	0.529	0.489	0.510	0.555	0.488	0.476	0.240	0.469
Annual Average	0.564	0.581	0.470	0.541	0.544	0.487	0.511	0.318	0.486

Month	Juana Diaz	Isabela	Lajas	Aguadilla	Ceiba	Guilarte	Carolina	Guanica	Maricao
January	0.640	0.595	0.486	0.532	0.473	0.192	0.526	0.495	0.360
February	0.651	0.616	0.543	0.549	0.486	0.236	0.540	0.525	0.382
March	0.664	0.598	0.601	0.545	0.516	0.187	0.576	0.562	0.284
April	0.553	0.411	0.531	0.484	0.424	0.167	0.542	0.490	0.254
May	0.579	0.593	0.510	0.526	0.470	0.152	0.556	0.510	0.193
June	0.534	0.535	0.491	0.505	0.437	0.163	0.544	0.517	0.211
July	0.542	0.556	0.496	0.536	0.469	0.155	0.535	0.527	0.281
August	0.481	0.531	0.534	0.511	0.458	0.161	0.542	0.509	0.224
September	0.579	0.508	0.518	0.531	0.464	0.193	0.543	0.483	0.307
October	0.600	0.572	0.569	0.526	0.474	0.193	0.539	0.595	0.314
November	0.626	0.624	0.592	0.508	0.450	0.193	0.484	0.532	0.404
December	0.566	0.593	0.581	0.507	0.461	0.194	0.473	0.613	0.371
Annual Average	0.584	0.561	0.538	0.522	0.465	0.182	0.533	0.530	0.299

Table 4.10: Calculated Diffuse Radiation (MJ/m^2)

Month	Ponce	Cabo Rojo	Mayaguez	Manati	Catano	San Juan	Fajardo	Río Grande	Gurabo
January	5.70	5.68	5.95	5.82	5.71	5.86	5.74	5.82	5.56
February	6.35	6.30	6.73	6.64	5.31	6.66	6.05	6.66	6.19
March	7.03	6.87	7.56	6.99	7.42	7.51	7.20	7.48	7.46
April	7.85	8.10	8.16	7.79	8.02	8.17	8.06	6.90	7.89
May	8.36	7.93	8.39	8.38	8.38	8.31	7.49	7.85	8.07
June	8.33	7.86	8.42	7.90	8.41	8.43	7.97	7.87	8.24
July	8.01	8.03	8.35	8.23	7.59	8.28	7.66	7.92	8.32
August	7.86	8.06	8.22	8.18	8.01	8.18	7.59	8.01	8.20
September	7.48	7.26	7.76	7.72	7.71	7.75	7.36	7.57	7.61
October	6.75	6.65	6.97	6.82	6.86	6.92	6.21	6.57	6.80
November	5.94	5.69	6.10	5.89	5.92	6.08	5.76	4.95	5.97
December	5.63	5.68	5.74	5.68	5.56	5.71	5.73	4.85	5.75
Annual Average	7.14	7.05	7.38	7.21	7.22	7.35	7.31	6.97	7.36

Month	Juana Diaz	Isabela	Lajas	Aguadilla	Ceiba	Guilarte	Carolina	Guanica	Maricao
January	5.38	5.62	6.00	5.86	5.99	4.54	5.89	5.99	5.85
February	5.97	6.20	6.62	6.56	6.74	5.67	6.60	6.68	6.66
March	6.54	7.11	7.09	7.40	7.50	5.63	7.25	7.33	6.87
April	7.94	8.12	8.03	8.15	8.15	5.64	7.99	8.14	7.07
May	8.01	7.93	8.32	8.28	8.39	5.53	8.16	8.32	6.33
June	8.26	8.27	8.38	8.37	8.41	5.76	8.24	8.31	6.70
July	8.18	8.13	8.33	8.23	8.37	5.52	8.22	8.24	7.56
August	8.20	8.08	8.07	8.15	8.22	5.60	8.04	8.14	6.74
September	7.41	7.68	7.67	7.62	7.75	5.88	7.57	7.75	7.24
October	6.55	6.67	6.72	6.85	6.96	5.29	6.82	6.59	6.56
November	5.62	5.59	5.83	6.08	6.16	4.65	6.12	6.08	6.12
December	5.57	5.40	5.51	5.68	5.75	4.37	5.73	5.35	5.65
Annual Average	7.03	7.14	7.25	7.27	7.38	5.37	7.23	7.28	6.76

Table 4.11: Calculated Beam Radiation (MJ/m^2)

Month	Ponce	Cabo Rojo	Mayaguez	Manati	Catano	San Juan	Fajardo	Río Grande	Gurabo
January	10.80	10.82	8.25	9.38	10.29	8.94	10.16	4.18	11.44
February	12.55	12.80	8.77	9.86	16.89	9.54	13.95	5.44	13.31
March	14.47	15.33	9.54	14.71	11.58	10.49	13.40	6.22	5.94
April	13.85	11.30	9.84	14.21	12.28	9.33	11.74	2.20	13.51
May	10.84	15.17	8.71	10.72	8.22	6.99	17.61	4.25	14.23
June	11.67	15.74	9.18	15.60	8.39	9.97	4.63	4.23	12.96
July	14.39	14.27	8.15	12.57	17.01	12.02	16.64	4.58	11.28
August	14.14	12.44	8.98	10.82	12.99	10.72	3.81	5.79	10.30
September	12.92	14.44	8.54	9.98	10.19	8.65	13.74	5.63	5.89
October	11.55	12.25	8.23	10.58	10.14	9.08	2.59	3.73	5.00
November	10.46	12.01	8.60	10.41	10.18	8.52	11.34	1.25	4.13
December	9.17	8.52	7.36	7.92	9.24	7.29	6.97	1.55	6.85
Annual Average	12.16	12.85	8.62	11.39	11.28	9.25	10.19	4.03	9.34

Month	Juana Diaz	Isabela	Lajas	Aguadilla	Ceiba	Guilarte	Carolina	Guanica	Maricao
January	12.52	10.88	7.60	8.94	7.21	0.86	8.71	7.91	4.25
February	14.53	13.10	10.48	10.64	8.56	1.73	10.30	9.92	5.34
March	16.86	13.99	14.11	11.80	10.70	0.97	13.05	12.47	3.13
April	13.06	7.48	12.17	10.25	7.95	0.66	12.61	10.46	2.53
May	14.59	15.27	11.58	12.32	10.01	0.47	13.54	11.58	1.17
June	12.64	12.73	10.82	11.43	8.69	0.64	13.06	11.89	1.60
July	12.92	13.57	10.97	12.67	9.93	0.48	12.68	12.26	3.34
August	10.20	12.22	12.33	11.35	9.28	0.60	12.66	11.36	1.86
September	13.49	10.62	11.03	11.48	9.05	1.12	12.03	9.65	3.86
October	12.95	11.83	11.78	10.15	8.44	1.01	10.58	12.71	3.64
November	12.38	12.21	11.17	8.42	6.74	0.85	7.68	9.22	5.48
December	9.63	10.40	10.09	7.82	6.55	0.83	6.87	11.15	4.35
Annual Average	12.97	11.96	11.15	10.63	8.62	0.83	11.17	10.82	3.24

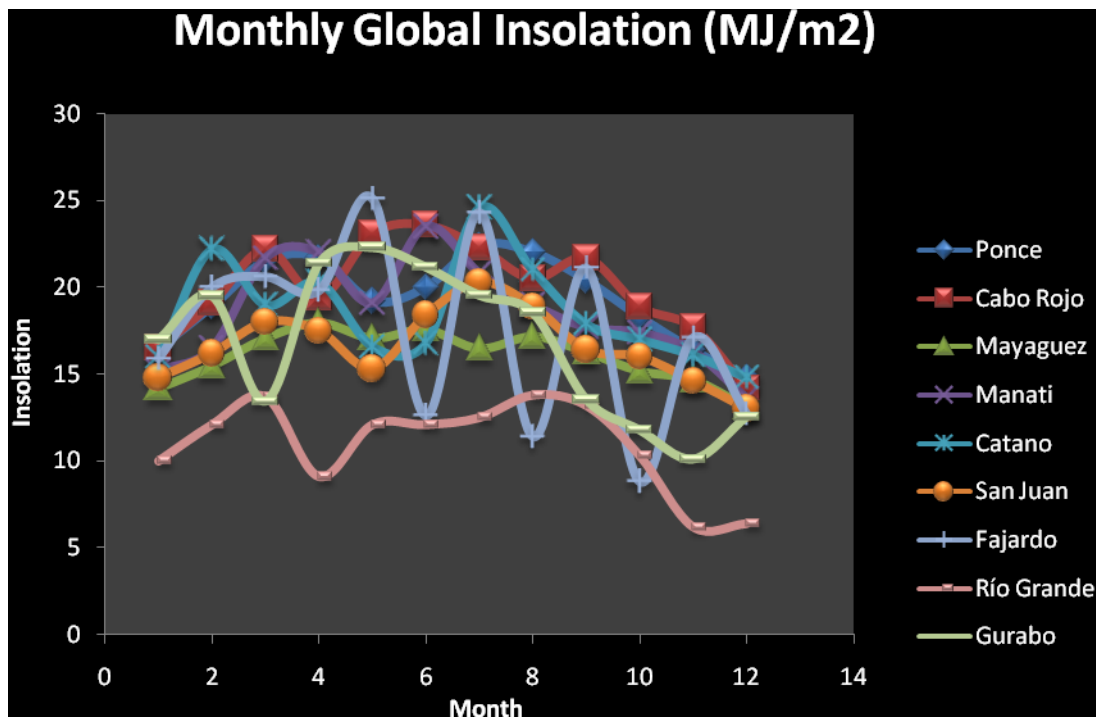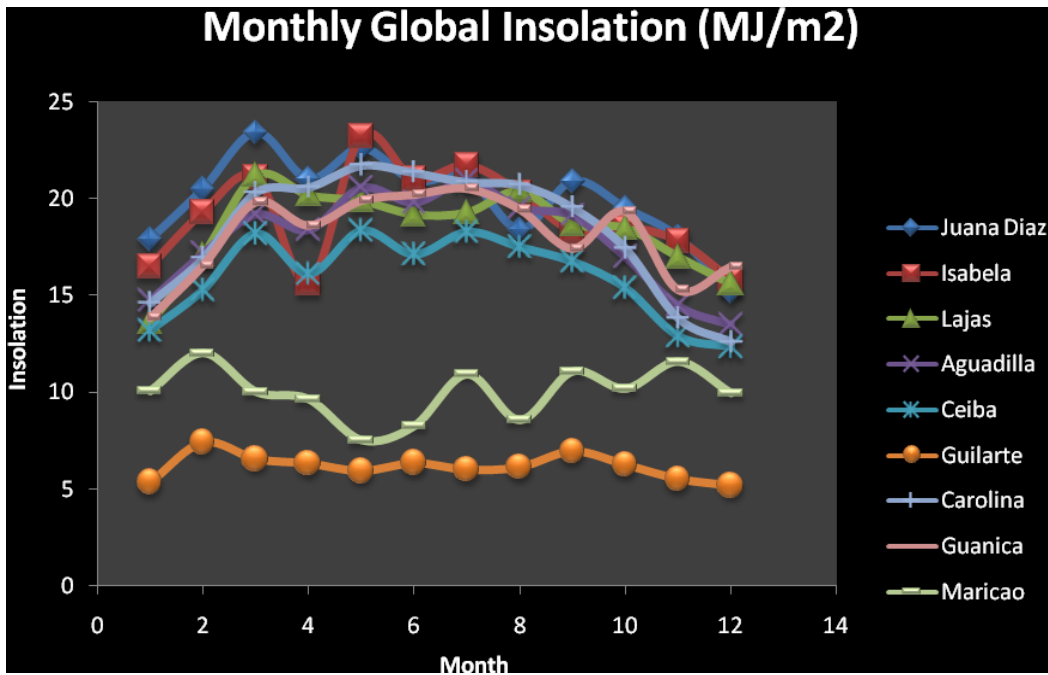## 4.7.2   Graphical Representation

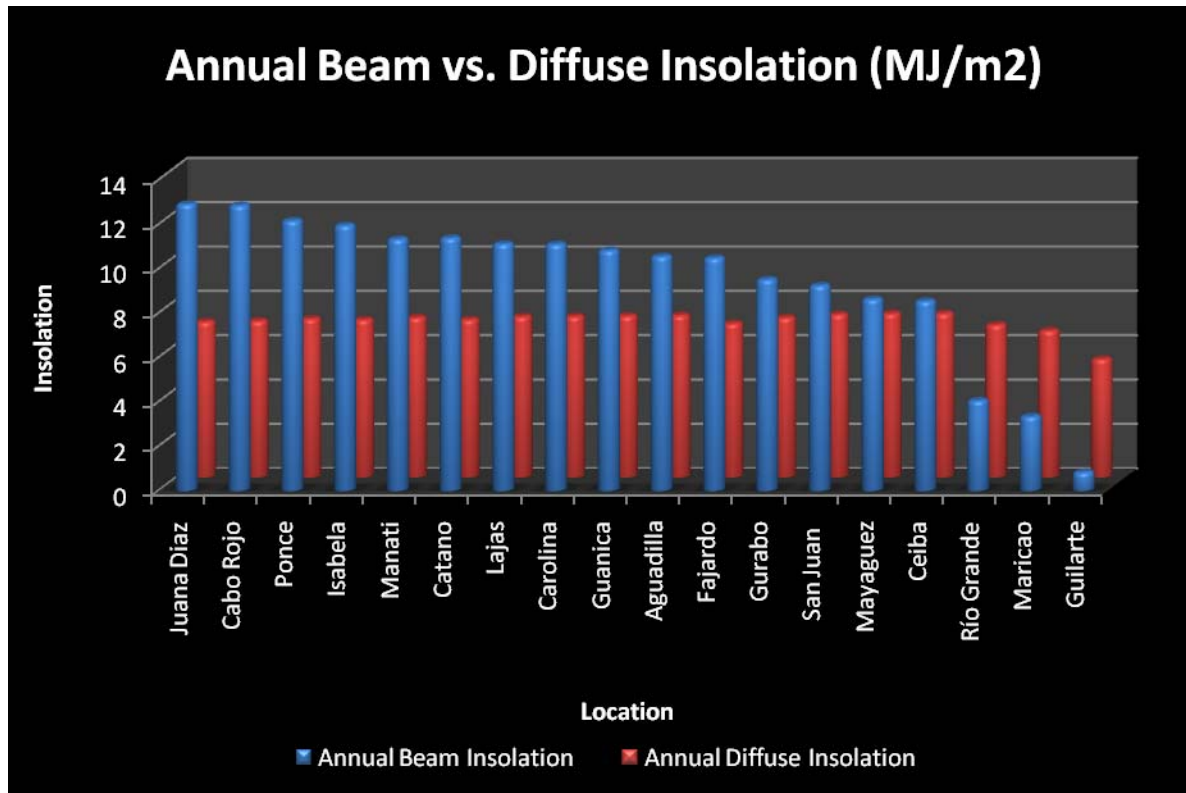Figure 4.4 Monthly global insolation for 18 sites in Puerto Rico.

Figure 4.5: Average Annual Beam and Diffuse Insolation Components

4.8 Solar Insolation Map for Puerto Rico

4.8.1 Insolation Map Reference

After compilation and processing of solar radiation data was completed for the eighteen sites we created a radiation map for Puerto Rico. Latitude and longitude information for each site was obtained using Google Earth®.

This map is similar to the one presented in (López and Soderstrom). In (López and Soderstrom) the authors had radiation data for six different locations. They calculated the ratio of average yearly radiation to average yearly extraterrestrial radiation (K_T) for these six locations and utilized linear regression to correlate it with the amount of annual rainfall in the locations. With the equation that resulted from this linear regression analysis, they calculated the average yearly radiation of other municipalities

in Puerto Rico using the average annual rainfall. Rainfall to K_T correlated by 94%. Their map is shown in Figure 4.6.
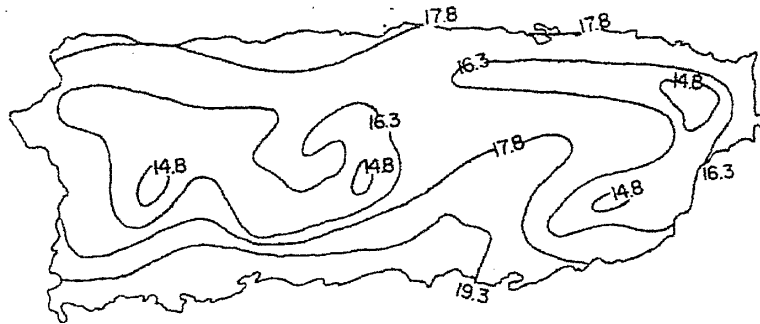

Figure 4.6 Average daily radiation map for Puerto Rico using K_T and rainfall correlation in (MJ/m^2)
(Source: López and Soderstrom [6])

Since we have data for more sites we used a different approach to generate our irradiation map for Puerto Rico, interpolation. Using spatial interpolation we generated an insolation matrix to construct the insolation map.

The data collected should not be interpolated linearly with respect to latitude, since there are very distinct climatic and geographical differences when moving from east to west along Puerto Rico. If longitude and latitude are to be considered we need a numerical analysis method.

The most frequent problem in modeling a physical phenomenon of this type is known as the scattered data interpolation problem. In general, data is collected at certain points that are scattered in space with no special structure. This type of problem normally contains two or more dimensions, that is, two or more independent variables. Examples of these are: interpolation of altimeter data, geoids, temperature, fluid dynamics and image processing.

There are well known straight-forward methods for solving one-dimensional problems, such as: linear, piecewise linear, polynomial or cubic interpolation. For greater dimension problems, some of these methods could be used but, are not so straight-

forward and require extensive algebraic manipulation, thus producing far larger systems of equations to be solved.

4.8.2   Methodology for Creating the Map

MATLAB® provides a function for solving this type of problem, giving the user the choice of several interpolation methods to be used: bilinear, bicubic, nearest or biharmonic (or bicubic) spline interpolation. All these methods were tested on the radiation data processed, being the biharmonic spline interpolation method the one that gave reasonable results.

The main problem with the other methods is that the function might return points on or very near the convex hull of the data as NaNs (Not a Number – usually division by zero). This is because roundoff in the computations makes it difficult to determine if a point near the boundary is in the convex hull. The "linear" and "nearest" methods also have discontinuities in the first and zero'th derivatives, respectively.

All methods, except biharmonic spline are based on a Delaunay triangulation of the data.

griddata, the MATLAB® function employed, requires several inputs which in the solar radiation case are: vectors for the data collected in terms of latitude, longitude and radiation. It also requires uniform grid vectors for the independent variables (latitude and longitude) for it to construct a "grid" in which the radiation data can be interpolated.

Figure 4.7 presents the resulting solar radiation map.

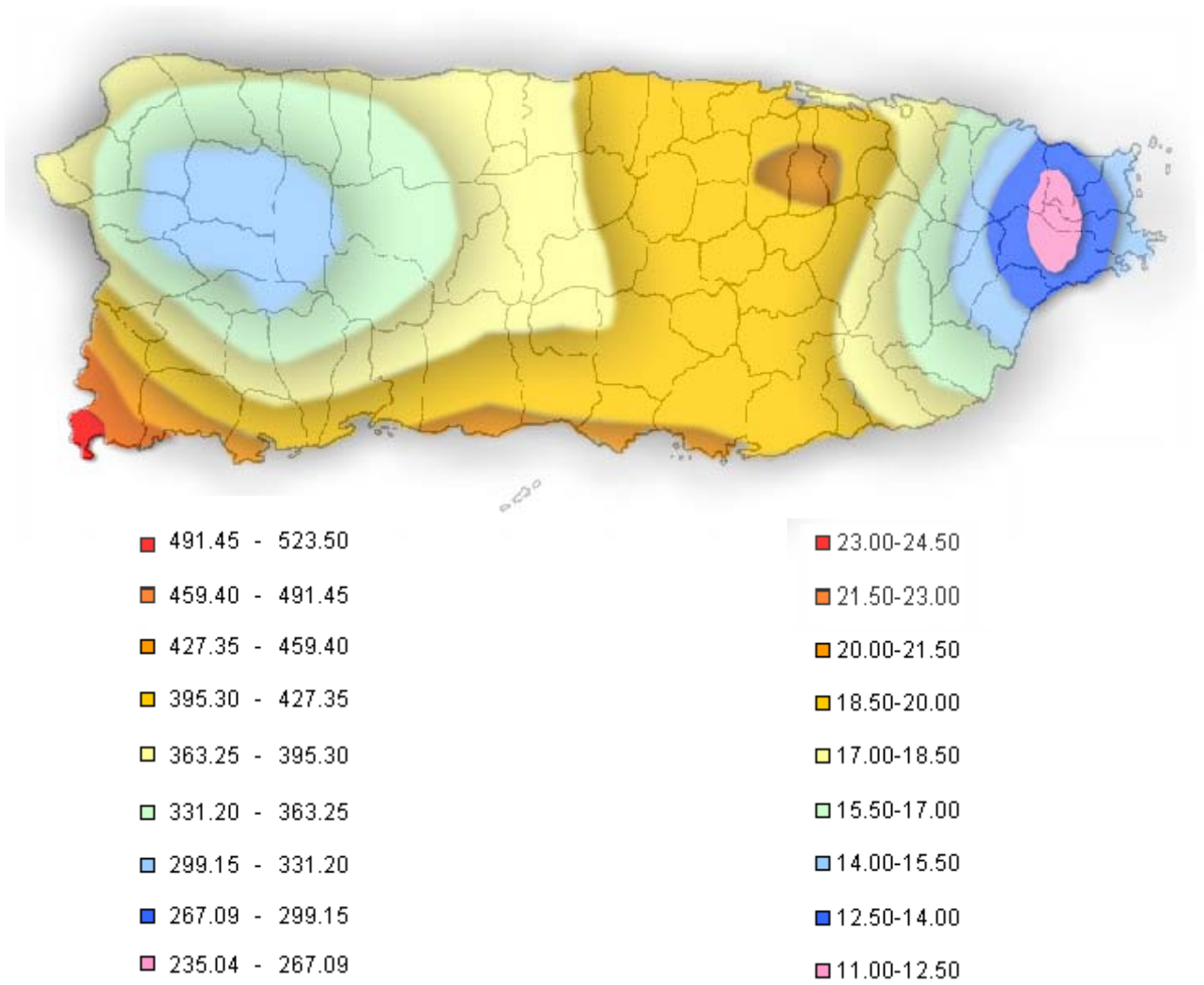|			
■ 491.45 - 523.50		■ 23.00-24.50	
■ 459.40 - 491.45		■ 21.50-23.00	
■ 427.35 - 459.40		■ 20.00-21.50	
■ 395.30 - 427.35		■ 18.50-20.00	
□ 363.25 - 395.30		□ 17.00-18.50	
□ 331.20 - 363.25		□ 15.50-17.00	
□ 299.15 - 331.20		□ 14.00-15.50	
■ 267.09 - 299.15		■ 12.50-14.00	
■ 235.04 - 267.09		■ 11.00-12.50	

Figure 4.7 Insolation Map for Puerto Rico in W/m^2 to the left and MJ/m^2 to the right

The radiation map shows that the most suitable locations for any type of solar system development lie in the south and in the extreme south-western tip of Puerto Rico. It also shows high radiation in Bayamón, Guaynabo, Toa Alta, Naranjito, Comerío and Aguas Buenas. Even though Bayamón, Guaynabo and Toa Alta present such high radiation levels, they are part of the metropolitan area and are highly populated. Although Naranjito, Comerío and Aguas Buenas appear to have high radiation levels, they lie in the base of La Cordillera Central which is a heavily wooded area and the environmental impact of a project there should be carefully considered. The south however is a somewhat dry and far less populated that can serve as a potentially favorable area for the development of solar systems.

4.8.3   Validating the Generated Insolation Map

To compare our work with the one by López and Soderstrom we have performed a correlation of the ratio of average yearly radiation to average yearly extraterrestrial radiation (K_T) with the amount of annual rainfall in the locations.

Using the data collected, K_T was computed for each of the fourteen locations and it was then correlated with their respective annual rainfalls as shown in Figure 4.8.
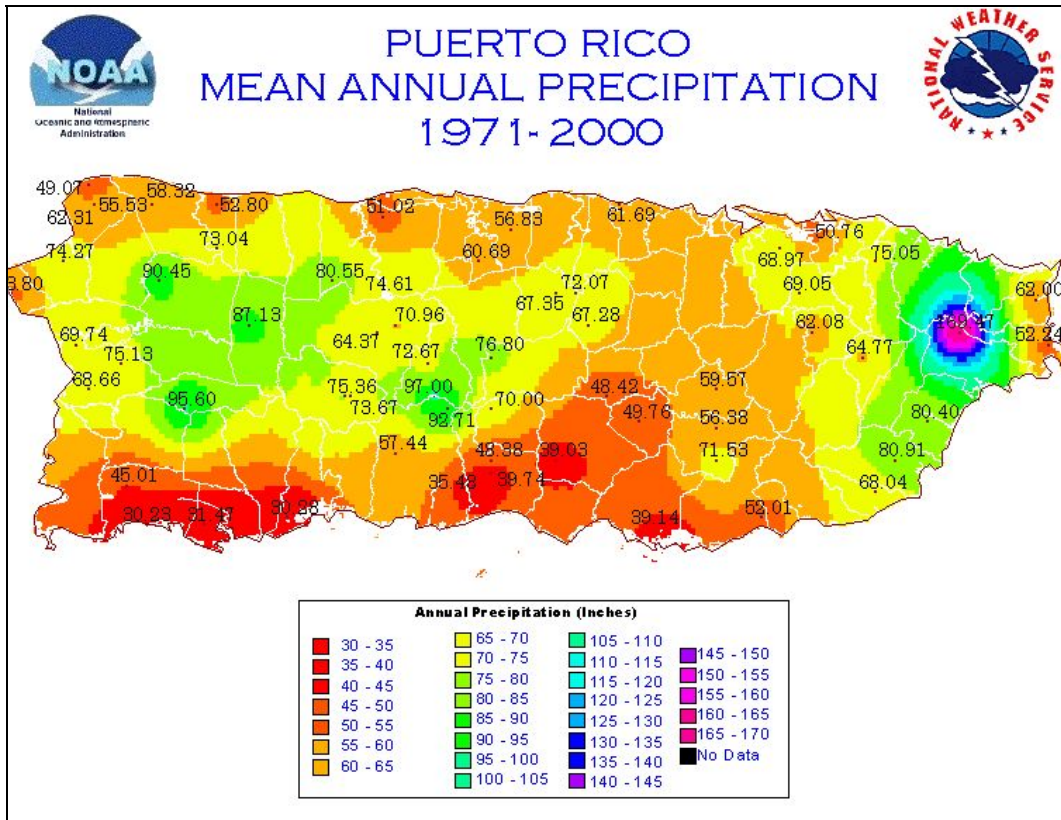
Figure 4.8: Mean annual precipitation data used for the regression analysis (Source: NOAA)

Our linear regression analysis provides a correlation between K_T and rainfall of 88.6%. This data appears in Table 4.12 and Figure 4.9.

Table 4.12 Data used for the linear regression analysis. Rainfall data was obtained from NOAA.

| Location	Annual Rainfall (in.)	Annual Rainfall (cm.)	K_T
Ponce	35.48	90.12	0.564
Cabo Rojo	45.01	114.33	0.581
Mayaguez	68.66	174.40	0.470
Manati	56.88	144.48	0.541
Catano	60	152.40	0.544
San Juan	68.97	175.18	0.487
Fajardo	62	157.48	0.511
Río Grande	130	330.20	0.318
Gurabo	62.08	157.68	0.526
Juana Diaz	39.74	100.94	0.584
Isabela	58.32	148.13	0.561
Lajas	30.23	76.78	0.538
Aguadilla	55.53	141.05	0.522
Ceiba	52.24	132.69	0.465
Guanica	31.47	79.93	0.530
Carolina	50.76	128.93	0.533
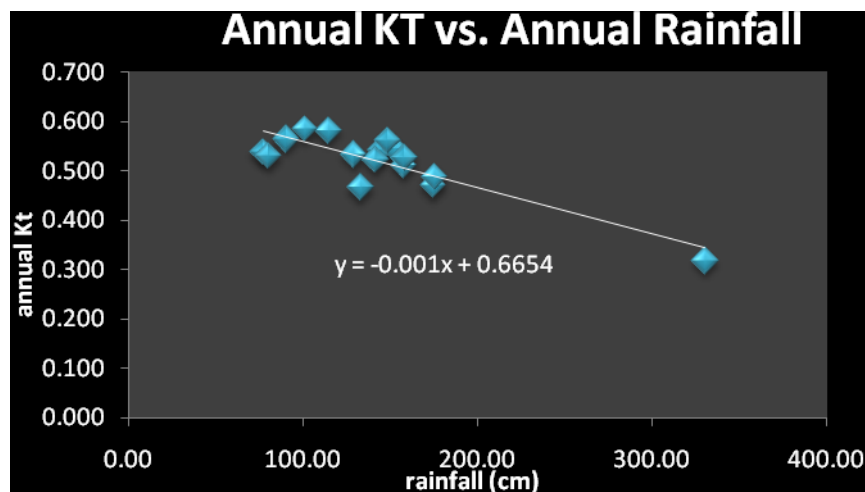
Figure 4.9: Linear fit output from Microsoft Excel®

We then used the equation from the regression analysis to corroborate the accuracy of the insolation map produced using MATLAB® Biharmonic Spline Interpolation Method. We used the locations for which we have rainfall measurements, namely; Guayanilla,

Lares, San Sebastian, Barranquitas, Aibonito, Adjuntas, Juncos and Arecibo. The average annual insolation obtained using the correlation equation fell within the insolation range presented in the insolation map for all cases. Table 4.13 summarizes the results of using the correlation method.

Table 4.13: Test data for testing the generated insolation
map obtained from linear regression

Location	Annual Rainfall (cm)	Average Annual Insolation (MJ/m2)
Guayanilla	99.416	19.430
Lares	221.310	15.245
San Sebastian	229.743	14.956
Barranquitas	122.987	18.621
Aibonito	126.390	18.504
Adjuntas	187.1218	16.419
Juncos	164.516	17.195
Arecibo	129.591	18.394

4.8.4   Insolation Map Limitations

There are limitations to the map we have developed due mainly to the fact that the data collected only represents eighteen municipalities in Puerto Rico and lie mainly in the coastal areas, meaning that locations in the interior part of the island are not well represented.

There is also a biasing factor in the data because several of the locations considered are forest areas. There is obviously a much lower radiation level if there are significant amounts of rainfall. Some of these locations are: Rio Grande (El Yunque), Gurabo, Guilarte and Maricao. Some of the insolation data from these locations was not considered when generating the insolation map for deeming them too low. It seems the instruments used to measure the sun were in the shadow!

Further work is needed to take measurements in the central, as well as in the southeastern part of Puerto Rico. Since our sources are from literature there is also some uncertainty regarding the uniformity of instrument calibration and data processing.

A more accurate Insolation Map for Puerto Rico could be developed in the future using our proposed approach and more data. This will surely benefit the development of solar technologies in Puerto Rico.

4.9   Solar Thermal Technologies Review

Solar Energy is the world's most abundant permanent source of energy. It is a clean and renewable energy that could discontinue our dependency of oil or other contaminants alternatives. There are several technologies in use to capture solar energy and use it; solar thermal production of electricity is one of them.

Solar Thermal Power Plants (STPPs) addressed in this study consist of two major components: a solar collector that converts solar radiation into thermal heat and a power conversion system that converts the heat into electricity.

There is a variety of solar and power conversion technologies that can be combined in different ways to produce electricity. STP plants produce electricity in the same way as conventional power stations, except they obtain part or all of their thermal energy input by concentrating solar radiation onto a receiver where heat transfer to a fluid takes place to drive a turbine or, alternatively, to move a piston in a sterling engine.

In this study, the solar thermal collection available technologies that will be considered are: parabolic troughs, power towers and parabolic dish.

Concentrating solar collectors are required to generate the elevated temperatures that can be used to efficiently power industrial and electric conversion processes. Unlike traditional power plants, concentrating solar power systems provide an environmentally benign source of energy, produce virtually no emissions, and consume no fuel other than sunlight.

About the only impact concentrating solar power plants have on the environment is land use. Although the amount of land a concentrating solar power plant occupies is larger than that of a fossil fuel plant, it can be argued the both types of plants use about the same amount of land because fossil fuel plants use additional land for mining and exploration as well as road building to reach the mines.

4.9.1   Parabolic Troughs

The collector field of these STPP consists of a large field of single-axis tracking parabolic trough solar collectors and the overall efficiency from collector to grid is about 15%.

The solar field is modular in nature and is composed of many parallel rows of solar collectors aligned on a north-south horizontal axis. Each solar collector has a linear parabolic-shaped reflector that focuses the sun's direct beam radiation on a linear receiver located at the focus of the parabola. The collectors track the sun from east to west during the day to ensure that the sun is continuously focused on the linear receiver.

A heat transfer fluid (HTF) is heated as it circulates through the receiver and returns to a series of heat exchangers in the power block where the fluid is used to generate high-pressure superheated steam. The superheated steam is then fed to a conventional reheat steam turbine/generator to produce electricity.

The spent steam from the turbine is condensed in a standard condenser and returned to the heat exchangers via condensate and feed water pumps to be transformed back into steam. Condenser cooling is provided by mechanical draft wet cooling towers. After passing through the HTF side of the solar heat exchangers, the cooled HTF is re-circulated through the solar field.

Historically, parabolic trough plants have been designed to use solar energy as the primary energy source to produce electricity. The plants can operate at full rated power using solar energy alone given sufficient solar input. During summer months, the plants typically operate for 10 to 12 hours a day at full-rated electric output.

However, to date, all plants have been hybrid solar/fossil plants; this means they have a backup fossil-fired capability that can be used to supplement the solar output during periods of low solar radiation. In the system shown in Appendix A, Figure 4.10, the optional natural-gas-fired HTF heater situated in parallel with the solar field, or the optional gas steam boiler/re-heater located in parallel with the solar heat exchangers, provide this capability. The fossil backup can be used to produce rated electric output during overcast or nighttime periods and if instead of fossil fuel we use biomass the plant remains a renewable generation endeavor.

4.9.1.1　　Some Solar Troughs History

Organized, large-scale development of solar collectors began in the U.S. in the mid-1970s under the Energy Research and Development Administration (ERDA) and continued with the establishment of the U.S. Department of Energy (DOE) in 1978.

Parabolic trough collectors capable of generating temperatures greater than 500°C (932°F) were initially developed for industrial process heat applications. Much of the early development was conducted by or sponsored through Sandia National Laboratories in Albuquerque, New Mexico. Numerous process heat applications, ranging in size from a few hundred to about 5000 m^2 of collector area, were put into service.

Acurex, SunTec, and Solar Kinetics were the key parabolic trough manufacturers in the United States during this period.

In 1983, Southern California Edison (SCE) signed an agreement with Acurex Corporation to purchase power from a solar electric parabolic trough power plant. Acurex was unable to raise financing for the project. Consequently, Luz negotiated similar power purchase agreements with SCE for the Solar Electric Generating System (SEGS) I and II plants. Later, with the advent of the California Standard Offer (SO) power purchase contracts for qualifying facilities under the Public Utility Regulatory Policies Act (PURPA), Luz was able to sign a number of SO contracts with SCE that led to the development of the SEGS III through SEGS IX projects. Initially, the plants were limited by PURPA to 30 MW in size; later this limit was raised to 80 MW. Appendix A, Table 4.16 shows the characteristics of the nine SEGS plants built by Luz.

4.9.1.2 Solar Troughs Collector Technology

The basic component of the solar field is the solar collector assembly (SCA). Each SCA is an independently tracking parabolic trough solar collector made up of parabolic reflectors (mirrors), the metal support structure, the receiver tubes, and the tracking system that includes the drive, sensors, and controls.

The general trend was to build larger collectors with higher concentration ratios (collector aperture divided by receiver diameter) to maintain collector thermal efficiency at higher fluid outlet temperatures. Luz System Three (LS-3) SCA: The LS-3 collector was the last collector design produced by Luz and was used primarily at the larger 80 MW plants.

The LS-3 collector represents the current state-of-the-art in parabolic trough collector design and is the collector that would likely be used in the next parabolic trough plant built. A more detailed description of the LS-3 collector and its components follows.

4.9.1.3   Luz Solar Trough (LS-3) System Description

The LS-3 reflectors are made from hot-formed mirrored glass panels, supported by the truss system that gives the SCA its structural integrity. The aperture or width of the parabolic reflectors is 5.76 m and the overall SCA length is 95.2 m (net glass).

The mirrors are made from a low iron float glass with a transmissivity of 98% that is silvered on the back and then covered with several protective coatings. The mirrors are heated on accurate parabolic molds in special ovens to obtain the parabolic shape. Ceramic pads used for mounting the mirrors to the collector structure are attached with a special adhesive. The high mirror quality allows 97% of the reflected rays to be incident on the linear receiver.

The linear receiver also referred to as a heat collection element (HCE), is one of the primary reasons for the high efficiency of the Luz parabolic trough collector design. The HCE consists of a 70 mm steel tube with a cermets selective surface, surrounded by an evacuated glass tube. The HCE incorporates glass-to-metal seals and metal bellows to achieve the vacuum-tight enclosure. The vacuum enclosure serves primarily to protect the selective surface and to reduce heat losses at the high operating temperatures.

The vacuum in the HCE is maintained at about 0.0001 mm Hg (0.013 Pa). The cermet coating is sputtered onto the steel tube to give it excellent selective heat transfer properties with an absorptivity of 0.96 for direct beam solar radiation, and a design emissivity of 0.19 at 350°C (662°F). The outer glass cylinder has anti-reflective coating on both surfaces to reduce reflective losses off the glass tube. Getters, metallic substances that are designed to absorb gas molecules, are installed in the vacuum space to absorb hydrogen and other gases that permeate into the vacuum annulus over time.

The SCAs rotate around the horizontal north-south axis to track the sun as it moves through the sky during the day. The axis of rotation is located at the collector center of mass to minimize the required tracking power. The drive system uses hydraulic rams to position the collector. A closed loop tracking system relies on a sun sensor for the precise alignment required to focus the sun on the HCE during operation to within +/- 0.1 degrees. The tracking is controlled by a local controller on each SCA. The local controller also monitors the HTF temperature and reports operational status, alarms, and diagnostics to the main solar field control computer in the control room.

The SCA is designed for normal operation in winds up to 25 mph (40 km/h) and somewhat reduced accuracy in winds up to 35 mph (56 km/h). The SCAs are designed to withstand a maximum of 70 mph (113 km/h) winds in their stowed position (the collector aimed 30° below eastern horizon). All of the existing Luz-developed SEGS projects were developed as independent power projects and were enabled through special tax incentives and power purchase agreements such as the California SO-2 and SO-4 contracts.

4.9.2   Power Towers

Power towers; consist of a central tower surrounded by a large array of mirrors known as heliostats. The heliostats are flat mirrors that track the sun on two axes (east to west and up and down). The heliostats reflect the sun's rays onto the central receiver. The sun's energy is transferred to a fluid: water, air, liquid metal and molten salt have been used.

This fluid is then pumped to a heat exchanger or directly to a turbine generator. Central receivers can achieve higher concentration ratios and therefore higher delivery temperatures than parabolic troughs (up to 565 °C). The solar collection efficiency is approximately 46% and the peak electrical conversion efficiency from solar radiation to electricity is 23%.

Several Central receiver demonstration projects have been constructed around the world and one commercial plant was built in Southern California: Solar One. Solar One was recently modified and is now referred to as Solar Two. Another commercial solar tower is currently in operation in Spain, the PS10, is discussed later.

Concentrating solar collectors, such as parabolic troughs and central receivers, can only concentrate direct solar radiation (as opposed to diffuse solar radiation). Thus, STPP will only perform well in very sunny locations, specifically the arid and semi-arid regions of the world. Although the tropics can have high solar radiation, the high diffuse solar radiation and long rainy seasons make these regions less desirable for STPP.

Although solar central receivers are less commercially mature than parabolic trough systems, approximately 10 solar central receiver systems have been constructed throughout the world. These are described in Table 4.14 Experimental Power Towers.

Table 4.14 Experimental Power Towers

Project	Country	Power Output (Mwe)	Heat transfer Fluid	Storage Medium	Operation Began
SSPS	Spain	0.5	Liquid Sodium	Sodium	1981
EURELIOS	Italy	1	Steam	Nitrate Salt/ Water	1981
SUNSHINE	Japan	1	Steam	Nitrate Salt/ Water	1981
SOLAR ONE	USA	10	Steam	Oil/ Rock	1982
CESA-1	Spain	1	Steam	Nitrate Salt	1983
MSEE/CAT B	USA	1	Molten Nitrate	Nitrate Salt	1984
THEMIS	France	2.5	Hi- Tec Salt	Hi- Tec Salt	1984
SPP-5	Russia	5	Steam	Water/ Steam	1986
TSA	Spain	1	Air	Ceramic	1993
SOLAR TWO	USA	10	Molten Nitrate Salt	Nitrate Salt	1996

Those experimental facilities were built to prove that solar power towers can produce electricity and to prove and improve on the individual system components. Most of these plants are research or proof-of-concept plants of only 1 to 2 MW.

Solar One in southern California was planned as a commercial project but at 10 MW, this project was really a pilot demonstration system. Solar One was built in 1981 and operated from 1982 to 1988. The plant used 1818 heliostats of 39.3 m^2 reflective area each to reflect sunlight onto a central receiver. Water was converted into steam and used to drive a 10 MW turbine.

The heat from the solar-heated steam could also be stored in a storage tank filled with rocks and sand using oil as the heat transfer fluid. The stored heat was used to generate power for up to four hours after sunset. This project proved the technical feasibility of the central receiver concept.

The system also had high reliability with 96% availability during sunlight hours. Solar One was redesigned in the early 1990's to overcome its limitations. The system heat transfer fluid was converted from water-steam to molten salt. Molten salt is inexpensive and allows for higher storage temperatures (290 °C). The main disadvantage is that it becomes solid below 220 °C and therefore must be maintained above this temperature. The receiver and storage tanks were replaced in order to use the new fluid. All pipes that carry the molten salt were heat-traced to avoid freezing the salt.

Solar Two began operation in November 1997 to encourage the development of molten-salt power towers, a consortium of utilities led by Southern California Edison joined with the U.S. Department of Energy to redesign the Solar One plant to include a molten-salt heat-transfer system.

The goals of the redesigned plant, called Solar Two, are to validate nitrate salt technology, to reduce the technical and economic risk of power towers, and to

stimulate the commercialization of power tower technology. Solar Two has produced 10 MW of electricity with enough thermal storage to continue to operate the turbine at full capacity for three hours after the sun has set. The heliostats have held up well over the almost 20 years that the plant has been in existence. Assuming success of the Solar Two project, the next plants could be scaled-up to between 30 and 100 MW in size for utility grid connected applications in the Southwestern United States and/or international power markets.

The cost and performance of central receiver systems are expected to improve significantly in the mid- and long-term. Because this technology is less mature than the parabolic trough, more dramatic improvements are expected. The first improvement in the performance of the central receiver system will be the addition of a selective surface on the receiver. The reduction of surface emissivity from 85% to 20% is expected to reduce heat losses by 60% and improve overall collection efficiency from 46% to 49%.

In the long-term, collector efficiency will increase to 52% through a 2% increase in receiver absorbtivity (94 to 96%), and higher mirror reflectivity because of improved coatings and better mirror washing. As the plants are made larger, the power cycle efficiency will improve slightly from 40 to 43%. The combination of larger plants, better operating procedures and higher solar capacity factor will reduce parasitic losses to keep the salt a liquid.

The costs of central receiver STPP are expected to drop significantly as this technology is commercialized. The largest cost reductions are expected with the heliostats. Heliostats represent approximately 50% of the total solar plant cost. Installation costs are only a few percent of the heliostat cost, so that these values can be assumed to be representative of installed costs.

For small production runs (in the order of a few hundred), a price of $180/m^2 is expected. A 100 MW plant (the medium-term) scenario would require 6000 heliostats and the price is expected to drop to $126/m^2 is anticipated. In the long-term at high production rates, the price is expected to fall to $70/m^2. Central receiver systems will benefit from the same cost reduction factors as described for the parabolic trough.

There is however greater uncertainty in the central receiver values because they are at an earlier stage in their development. Because of the large reduction in heliostat costs, central receiver systems show a 63% reduction in cost-per-kilowatt (current 30 MW to a long-term 200 MW). In the long-term, Central Receiver systems are predicted to have a 25% lower cost than parabolic trough systems. The prime reason for the lower cost is the reduction of piping. Parabolic trough systems must use insulated piping to connect all the collector arrays. Central receivers concentrate and collect the heat by reflecting the solar radiation to a central source.

4.9.2.1 PS10 - the Most Recently Power Tower Commercial Installation

PS10 is a 10 MWe (MW electric as opposed to MWt or Mw thermal) Concentrating Solar Thermal (CST) power plant with an investment of approximately $30 million dollars (see Appendix B, Figure 4.11, Figure 4.12,

Table 4.17 and Table 4.18). The Solar Plant works with direct saturated steam generation, at low values of temperature and pressure (250°C @ 40bar).

The PS10 is operating near the sunny southern Spanish city of Seville and is the first of a set of solar plants that will be constructed until 2013 of a very ambitious project that will feed with electricity all the city of Seville and will reach a total production of 300 MW. PS10 heliostat field is composed by 624 heliostats for a total reflective surface of 75.216m^2. It is arranged in 35 circular rows around the tower. Each heliostat, Sanlucar

120 type, is a mobile 120 m² curved reflective surface mirror that concentrates solar radiation on a receiver at the top of a 100 m tower.

At the top of the tower is the receiver. The receiver is the system where concentrated solar radiation energy is transferred to the working fluid to increase enthalpy. PS10 receiver is based on cavity concept to reduce as much as possible radiation and convection losses. The receiver is basically a forced circulation radiant boiler with low ratio of steam at the panels output, in order to ensure wet inner walls in the tubes. Special steel alloys have been used for its construction in order to operate under important heat fluxes and possible high temperatures. It has been designed to produce above 100.000 kg/h of saturated steam at 40bar- 250°C from thermal energy supplied by concentrated solar radiation flux. It is formed by 4 vertical panels 5.40m width x 12.00m height each one to conform an overall heat exchange surface of about 260m². These panels are arranged into a semi-cylinder of 7.00m of radius.

Turbine generator produces 11 MWe gross and 10 MWe net with 30% efficiency. Annual performance produce 22.1 GWh gross (12% efficiency) and 19.2 GWh net (10.5% efficiency), being equivalent to almost 2000 hours of equivalent nominal production (22% Capacity Factor).

For cloud transients, the plant has a 20-MWh thermal capacity saturated water thermal storage system (equivalent to 50 minutes of 50% load operation). The system is made up of 4 tanks that are sequentially operated in order of their charge status. During full-load plant operation, part of the 250°C/40 bar steam produced by the receiver is employed to load the thermal storage system. When energy is needed to cover a transient period, the energy is recovered from the saturated water at 20 bar to run the turbine at 50% load.

The tower was designed to reduce the visual impact of such a tall structure (115 m total height), so the body of the tower is rather thin (8 m) when seen from the side.

The front needs to be about 18 m wide to allocate the 14 m wide receiver. A large space has been left open in the body of the tower to give the sensation of a lightweight structure. An accessible platform at a height of 30 m provides visitors with a good view of the heliostat field lying north of the tower.

4.9.3   Parabolic Dish

Dish- engine systems convert the thermal energy in solar radiation to mechanical energy and then to electrical energy in much the same way that conventional power plants convert thermal energy from combustion of a fossil fuel to electricity. Dish-engine systems use a mirror array to reflect and concentrate incoming direct normal insolation to a receiver, in order to achieve the temperatures required to efficiently convert heat to work. This requires that the dish track the sun in two axes that is the collector aperture will always be normal to the sun.

Tracking in two axes is accomplished in one of two ways, *(1) azimuth-elevation tracking;* the collector aperture must be free to rotate about the zenith axis and an axis parallel to the surface of the earth. The tracking angle about the zenith is the solar azimuth angle, and the tracking angle about the horizontal axis is the solar altitude angle and *(2) polar tracking;* one axis of rotation is aligned parallel to the earth's rotational pole, that is, aimed toward the star Polaris. This gives it a tilt from the horizon equal to the local latitude angle, so the tracking angle about the polar axis is equal to the sun's hour. The collector rotates at a constant rate of 15°/ hr to match the rotational speed of the earth. The other axis of tracking, the declination axis, is perpendicular to the polar axis. Movement about this axis occurs slowly and varies by +/- 23½° over a year. Most of the smaller dish/engine systems have used this method of tracking.

A reflective surface, metalized glass or plastic, reflects incident solar radiation to a small region called the focus. The size of the solar concentrator for dish- engine systems is determined by the engine. At a nominal maximum direct normal solar insolation of 1000 W/m^2, a 25-kW dish- Stirling system's concentrator has a diameter of approximately 10 meters. Concentrators use a reflective surface of aluminum or silver, deposited on glass or plastic. The most durable reflective surfaces have been silver/glass mirrors, similar to decorative mirrors used in the home. Attempts to develop low-cost reflective polymer films have had limited success. Because dish concentrators have short focal lengths, relatively thin glass mirrors (thickness of approximately 1 mm) are required to accommodate the required curvatures. In addition, glass with low-iron content is desirable to improve reflectance. Depending on the thickness and iron content, silvered solar mirrors have solar reflectance values in the range of 90 to 94%.

The ideal concentrator shape is a parabolic of revolution. Some solar concentrators approximate this shape with multiple, spherically-shaped mirrors supported with a truss structure (See Appendix C, Figure 4.13). An innovation in solar concentrator design is the use of stretched-membranes in which a thin reflective membrane is stretched across a rim or hoop. A second membrane is used to close off the space behind. A partial vacuum is drawn in this space, bringing the reflective membrane into an approximately spherical shape. The concentrator's optical design and accuracy determine the concentration ratio.

The base-year technology (1997) is represented by the 25 kW dish-Stirling system developed by McDonnell Douglas (MDA) in the mid 1980s. Similar cost estimates have been predicted for the Science Applications International Corporation (SAIC) system with the STM 4-120 Stirling engine. Southern California Edison Company operated a MDA system on a daily basis from 1986 through 1988. During its last year of operation, it achieved an annual efficiency of 12%- 23% despite significant unavailability caused by spare part delivery delays. This annual efficiency is better than what has been achieved by all other solar electric systems, including photovoltaic, solar thermal

troughs, and power towers, operating anywhere in the world. The base-year peak and daily performance of near-term technology are assumed to be that of the MDA systems. System costs assume construction of eight units. Operation and maintenance (O&M) costs are of the prototype demonstration and accordingly reflect the problems experienced.

4.9.3.1   Parabolic Dish Receivers

The receiver absorbs energy reflected by the concentrator and transfers it to the engine's working fluid. The absorbing surface is usually placed behind the focus of the concentrator to reduce the flux intensity incident on it. An aperture is placed at the focus to reduce radiation and convection heat losses. Each engine has its own interface issues.

Stirling engine receivers must efficiently transfer concentrated solar energy to a high-pressure oscillating gas, usually helium or hydrogen. In Brayton receivers the flow is steady, but at relatively low pressures. There are two general types of Stirling receivers, direct-illumination receivers (DIR) and indirect receivers which use an intermediate heat-transfer fluid.

Directly-illuminated Stirling receivers adapt the heater tubes of the Stirling engine to absorb the concentrated solar flux. Because of the high heat transfer capability of high-velocity, high-pressure helium or hydrogen, direct-illumination receivers are capable of absorbing high levels of solar flux (approximately 75 W/cm2). However, balancing the temperatures and heat addition between the cylinders of a multiple cylinder Stirling engine is an integration issue.

Solar receivers for dish/Brayton systems are less developed. In addition, the heat transfer coefficients of relatively low pressure air along with the need to minimize pressure drops in the receiver make receiver design a challenge. The most successful

Brayton receivers have used "volumetric absorption" in which the concentrated solar radiation passes through a fused silica "quartz" window and is absorbed by a porous matrix. This approach provides significantly greater heat transfer area than conventional heat exchangers that utilize conduction through a wall.

4.9.3.2 Parabolic Dish Engines

The engine in a dish- engine system converts heat to mechanical power in a manner similar to conventional engines, by compressing a working fluid when it is cold, heating the compressed working fluid, and then expanding it through a turbine or with a piston to produce work.

The mechanical power is converted to electrical power by an electric generator or alternator. A number of thermodynamic cycles and working fluids have been considered for dish- engine systems. These include Rankine cycles, using water or an organic working fluid; Brayton, both open and closed cycles; and Stirling cycles.

Other, more exotic thermodynamic cycles and variations on the above cycles have also been considered. The heat engines that are generally favored use the Stirling and open Brayton (gas turbine) cycles. The use of conventional automotive Otto and Diesel engine cycles is not feasible because of the difficulties in integrating them with concentrated solar energy. Heat can also be supplied by a supplemental gas burner to allow operation during cloudy weather and at night. Electrical output in the current dish- engine prototypes is about 25 kWe for dish- stirling systems and about 30 kW for the Brayton systems under consideration.

Smaller 5 to 10 kWe dish- stirling systems have also been demonstrated. Stirling cycle engines used in solar dish- stirling systems are high-temperature, high-pressure externally heated engines that use a hydrogen or helium working gas. Working gas temperatures of over 700°C (1292F) and as high as 20 MPa are used in modern high-

performance stirling engines. In the stirling cycle, the working gas is alternately heated and cooled by constant-temperature and constant-volume processes. Stirling engines usually incorporate an efficiency-enhancing regenerator that captures heat during constant-volume cooling and replaces it when the gas is heated at constant volume.

There are a number of mechanical configurations that implement these constant-temperature and constant-volume processes. Most involve the use of pistons and cylinders. Some use a displacer (a piston that displaces the working gas without changing its volume) to shuttle the working gas back and forth from the hot region to the cold region of the engine.

4.9.3.3   Parabolic Dish for Utility Application

Because of their versatility and hybrid capability, dish- engine systems have a wide range of potential applications. In principle, dish- engine systems are capable of providing power ranging from kilowatts to gigawatts. However, it is expected that dish-engine systems will have their greatest impact in grid-connected applications in the 1 to 50 MWe power range.

Their ability to be quickly installed, their inherent modularity, and their minimal environmental impact make them a good candidate for new peaking power installations. The output from many modules can be ganged together to form a dish- engine farm and produce a collective output of virtually any desired amount.

In addition, systems can be added as needed to respond to demand increases. Although dish- engine systems do not currently have a cost-effective energy storage system, their ability to operate with fossil or bio-derived fuels makes them, in principal, fully dispatchable. This capability in conjunction with their modularity and relatively

benign environmental impacts suggests that grid support benefits could be a major advantage of these systems.

4.10 Thermal Technologies Comparison

Table 4.15 Technologies Comparison summarizes features of the three solar technologies discussed above in the solar thermal technologies review. Towers and Troughs are best for large grid power projects in the range of 30-200 MW although dish- engine systems can be used in single or grouped applications. The most mature technology available is the parabolic trough that has various commercially systems as the 354 MW operating in the Mojave Desert in California. Power Towers and Parabolic Dish offer the opportunity to achieve higher solar- to- electric efficiencies and lower cost than parabolic troughs. Table 4.19 provides a summary of costs and performance indicators for these technologies.

Table 4.15 Technologies Comparison

	Parabolic Troughs	Power Towers	Parabolic Dish
Large Grid Applications	x	x	
Modular Applications			x
Most Mature Technology	x		
Offer Better Efficiency		x	x

References:

[1]   Briscoe, C.B. *Weather in the Luquillo Mountains of Puerto Rico*, Institute of Tropical Forestry, U.S. Department of Agriculture, Puerto Rico, 1966.

[2]   Collares-Pereira, M. & Rabl, A., *The Average Distribution of Solar Radiation – Correlations Between Diffuse and Hemispherical and Between Daily and Hourly Insolation Values*, Solar Energy, Vol. 22, pp. 155-164, 1979.

[3]   Duff, W., *A Methodology for Selecting Optimal Components for Solar Thermal Energy Systems: Application to Power Generation*, Solar Energy, Vol. 17, pp. 245-254, 1975.

[4]   Duffie, J. & Beckman, W. *Solar Engineering of Thermal Processes*, John Wiley & Sons, 2006.

[5]   Gaspar, C., *Multigrid Technique for Biharmonic Interpolation with Application to Dual and Multiple Reciprocity Method*, Numerical Algorithms, Vol. 21, pp. 165-183, 1999.

[6]   López, A.M. & Soderstrom, K.G. *Insolation in Puerto Rico*, Journal of Solar Energy Engineering, 1983.

[7]   National Solar Radiation Database User's Guide (1961-1990) http://rredc.nrel.gov/solar/pubs/NSRDB/NSRDB_index.html

[8]   *NOAA Website* (http://www.srh.noaa.gov/sju/climate_normals.html)

[9]   Sandwell, David T., *Biharmonic Spline Interpolation of GEOS-3 and SEASAT Altimeter Data*, Geophysical Research Letters, 14, 2, 139-142, 1987.

[10]   Shapira, Y. *Matrix-Based Multigrid: Theory and Applications*, Kluwer Academic Publishers, 2003.

[11]   Tveito, A. & Winther, R. *Introduction to Partial Differential Equations: A Computational Approach*, Springer, 2005.

[12]   Wikipedia contributors, 'Solar energy', Wikipedia, The Free Encyclopedia, http://en.wikipedia.org/w/index.php?title=Solar_variation&oldid=176881574 [accessed 9 December 2007].

[13]   Yang, W.Y., Cao, W., Chung, T. & Morris, J. *Applied Numerical Methods Using MATLAB®*, John Wiley & Sons, 2005.

[14]   ABENGOA SOLAR Website, (http://www.abengoa.es/), September 15, 2007.

[15]   ABENGOA SOLAR Website, PS10 "The First Solar Commercial Tower", http://www.solucar.es/sites/solar/es/nproyectos_ps10.jsp, November 21, 2007.

[16] Monografias Contributors, PS10: A 10 MW Solar Tower Power Plant for Southern Spain, http://www.euro-energy.net/success_stories/52.html, October 17, 2007.

[17] Solar Paces Website, "How Works the Concentrating Solar Power Plants", http://www.solarpaces.org/CSP_Technology/csp_technology.htm, December 11, 2007.

[18] Solar Paces, Concentrating Solar Power Plants, Technology Characterization Solar Power Towers PDF, October 10, 2007.

[19] Enermodal Engineering Ltd./Marbek Resource Consultants, Cost Reduction Study For Solar Thermal Power Plants, September 15, 2007.

[20] Solar Paces, Concentrating Solar Power Plants, Technology Characterization Solar Power Trough System PDF, October 10, 2007.

[21] NREL'S Strategic Energy Analysis Center, Power Technologies Energy Data Book, Fourth Edition, Chapter 2.

[22] Solar Paces, Concentrating Solar Power Plants, Technology Characterization Solar Dish System PDF, October 10, 2007

[23] DOE website, "Renewable Energy Technology Characterization, www.doe.gov, December 18, 2007.

[24] Robert A. Rohde, http://www.globalwarmingart.com/wiki/Image:Solar_Cycle_Variations_png.

Appendix A: Solar Troughs
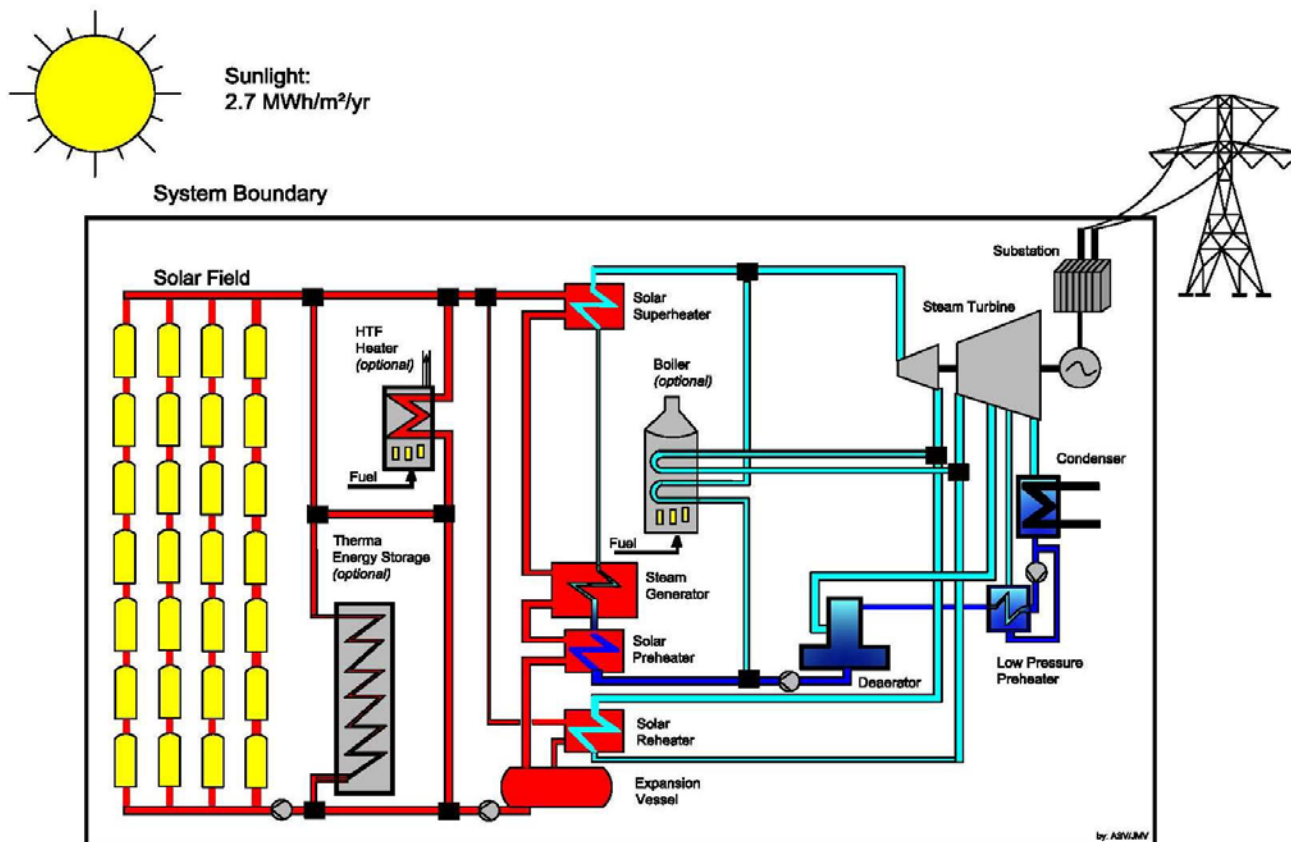
Figure 4.10 Solar/Rankine Parabolic Trough System Diagram (Source: Adapted from [20])

Table 4.16 Characteristics of SEGS I through IX

SEGS Plant	1st Year of Operation	Net Output (Mw$_e$)	Solar Field Outlet Temp. (°C/°F)	Solar Field Area (m^2)	Solar Turbine Eff. (%)	Fossil Turbine Eff. (%)	Annual Output (MWh)
I	1985	13.8	307/585	82,960	31.5	-	30,100
II	1986	30	316/601	190,338	29.4	37.3	80,500
III & IV	1987	30	349/660	230,300	30.6	37.4	92,780
V	1988	30	349/660	250,500	30.6	37.4	91,820
VI	1989	30	390/734	188,000	37.5	39.5	90,850
VII	1989	30	390/734	194,280	37.5	39.5	92,646
VIII	1990	30	390/734	464,340	37.6	37.6	252,750
IX	1991	30	390/734	483,960	37.6	37.6	256,125

Appendix B: Power Tower PS10
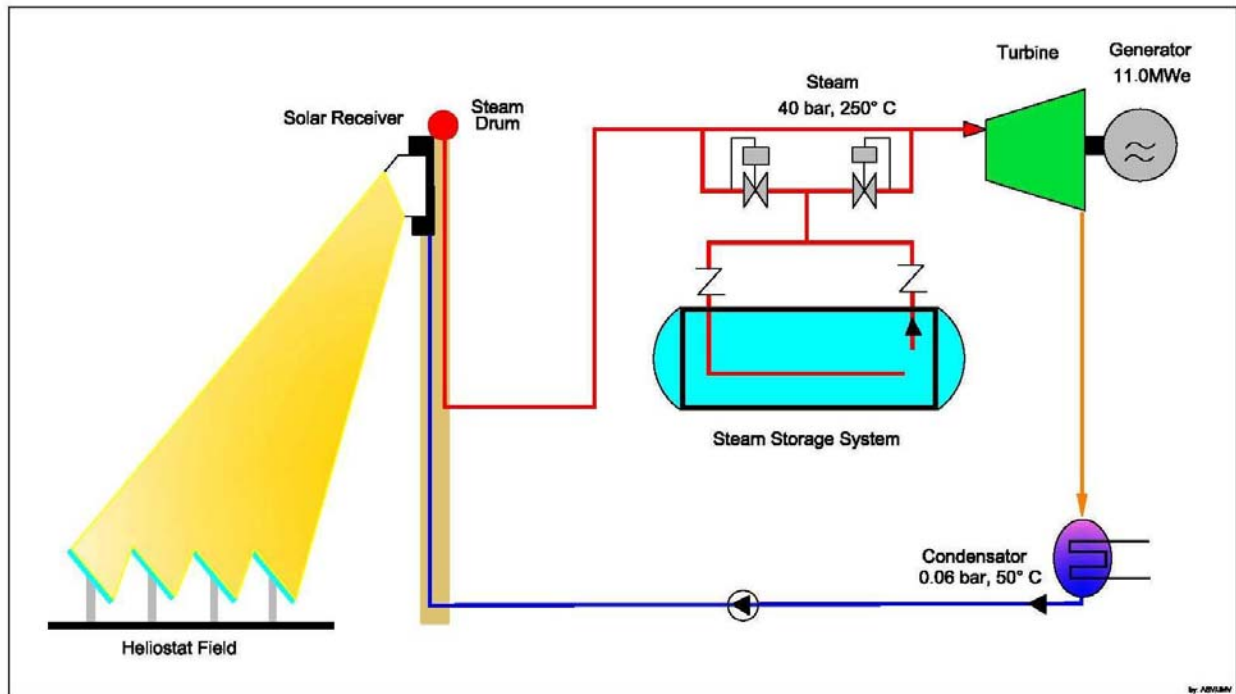
Figure 4.11 PS10 Diagram (Source: Adapted from [15])

Figure 4.12 PS10 Tower and heliostats (Used with permission:
http://creativecommons.org/licenses/by/2.0/)

Table 4.17 PS10 Design Parameters (Source: Adapted from [15])

Solar Plant Design Parameters	
Annual Irradiation $|kWh/m^2|$	2063
Design Point Day	355 (noon)
Design Point Irradiance $|W/m^2|$/Design Point Power $|MWe|$	850/10
Solar Multiple	1.15
Tower Height $|m|$	100
Heliostats Number/Heliostat Reflective Surface $|m^2|$	624/76
Receiver Shape $|m|$	Half Cylinder
Receiver diameter $|m|$/Receiver Height $|m|$	10.5/10.5

	Design Point	Annual Balance
Power/Energy onto Reflective Surface	75.88 MW	183.50 GWh
Heliostat Field Optic Efficiency	0.729	0.647
Gross Power/Energy onto Receiver	55.27 MW	118.72 GWh
Receiver and Air Circuit Efficiency	0.740	0.614
Power/Energy to Working Fluid	40.92 MW	72.90 GWh
Power/Energy to Storage	5.34 MW	
Power/Energy to Turbine	35.58 MW	72.90 GWh
Thermal->Electric Efficiency	0.309	0.303
Gross Electric Power/Energy	11.00 MW	22.09 GWh
Net Electric Power/Energy	10.00 MW	19.20 GWh

Table 4.18 PS10 Equipment Cost (Source: Adapted from [15])

Cost PS10	Investment (Thousand $)
General Coordination	178
Civil Works	657
Heliostats	9,678
Tower	1,876
Receiver + Storage + Steam Gen.	9,581
EPGS	4,803
Control	781
Total	27,553

Appendix C: Parabolic Dish
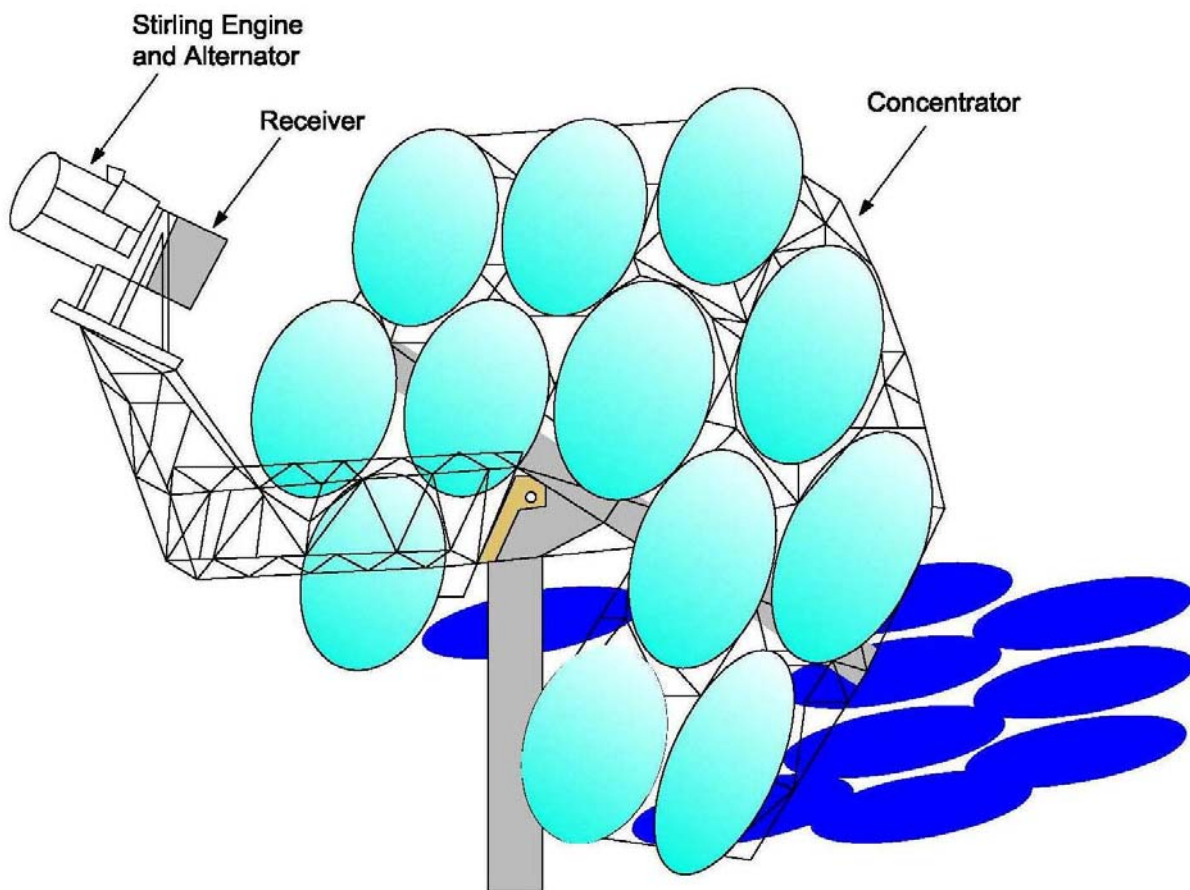
Figure 4.13 Dish- Stirling System Schematic (Source: Adapted from [22])

Table 4.19 Performance and Cost indicators [20, 27]

Indicator		1980's Prototype		Hybrid System		Commercial Engine		Heat Pipe Receiver		Highest Production		Highest Production	
		1997		2000		2005		2010		2020		2030	
Name	Units		+/-%		+/-%		+/-%		+/-%		+/-%		+/-%
Typical Plant Size, MW	MW	0.025		1	50	30	50	30	50	30	50	30	50
Performance													
Capacity Factor	%	12.4		50		50		50		50		50	
Solar Fraction	%	100		50		50		50		50		50	
Dish module rating	kW	25		25		25		27.5		27.5		27.5	
Per Dish Power Production	MWh/yr/dish	27.4		109.6		109.6		120.6		120.6		120.6	
Capital Cost													
Concentrator	$/kW	4,200	15	2,800	15	1,550	15	500	15	400	15	300	15
Receiver		200	15	120	15	80	15	90	15	80	15	70	15
Hybrid		-----		500	30	400	30	325	30	270	30	250	30
Engine		5,500	15	800	20	260	25	100	25	90	25	90	25
Generator		60	15	50	15	45	15	40	15	40	15	40	15
Cooling System		70	15	65	15	40	15	30	15	30	15	30	15
Electrical		50	15	45	15	35	15	25	15	25	15	25	15
Balance of Plant		500	15	425	15	300	15	250	15	240	15	240	15
Subtotal (A)		10,580		4,805		2,710		1,360		1,175		1,045	
General Plant Facilities (B)		220	15	190	15	150	15	125	15	110	15	110	15
Engineering Fee, 0.1*(A+B)		1,080		500		286		149		128		115	
Project/ Process Contingency		0		0		0		0		0		0	
Total Plant Cost		11,880		5,495		3,146		1,634		1,413		1,270	
Prepaid Royalties		0		0		0		0		0		0	

Name	Units	1980's Prototype		Hybrid System		Commercial Engine		Heat Pipe Receiver		Highest Production		Highest Production	
		1997		2000		2005		2010		2020		2030	
			+/-%		+/-%		+/-%		+/-%		+/-%		+/-%
Init Cat & Chem. Inventory		120	15	60	15	12	15	6	15	6	15	6	15
Starup Costs		350	15	70	15	35	15	20	15	18	15	18	15
Other		0		0		0		0		0		0	
Inventory Capital		200	15	40	15	12	15	4	15	4	15	4	15
Land, @$16,250/ha		26		26		26		26		26		26	
Subtotal		696		196		85		56		54		54	
Total Capital Requirement		12,576		5,691		3,231		1,690		1,467		1,324	
Total Capital Req. w/o Hybrid		12,576		5,191		2,831		1,365		1,197		1,074	
Operation and Maintenance Cost													
Labor	¢/kWh	12	15	2.1	25	1.2	25	0.6	25	0.55	25	0.55	25
Material	¢/kWh	9	15	1.6	25	1.1	25	0.5	25	0.5	25	0.5	25
Total	¢/kWh	21		3.7		2.3		1.1		1.05		1.05	

The Columns for "+/-%" refer to uncertainty associated with a given estimate.
The construction period is assumed to be <1 year for a MW scale system.